



Research paper

Mechanical design and friction modelling of a cable-driven upper-limb exoskeleton

Miha Dežman^{a,*}, Tamim Asfour^a, Aleš Ude^b, Andrej Gams^b

^a High Performance Humanoid Technologies (H2T), Institute for Anthropomatics and Robotics (IAR), Karlsruhe Institute of Technology (KIT), Adenauerring 2, 76131 Karlsruhe, Germany

^b Department of Automation, Biocybernetics and Robotics, Jožef Stefan Institute, Jamova 39, 1000 Ljubljana, Slovenia



ARTICLE INFO

Keywords:

Upper-limb exoskeleton
 Mechanical design
 Rapid-prototyping
 Bowden-cable transmission
 Bowden-cable adhesion
 Friction modelling
 Friction identification
 Actuator parameter identification

ABSTRACT

This paper presents a lightweight and low-inertia cable-driven upper-limb exoskeleton powerful enough to meet the requirements for activities of daily living. It presents the mechanical design, kinematic structure, the underlying actuation system, sensors, other electronic components as well as the controller of the exoskeleton.

The extensive effect of friction on cable-driven designs, such as the one presented in this paper, requires proper mathematical modelling for controller design. Thus, we propose a current actuator model that describes the relationship between the motor current, velocity, and external load. The model relies on an underlying Stribeck+Coulomb friction representation and an additional parameter that modifies its Coulomb friction representation with an offset to represent adhesion between a cable and sheath.

The model has been validated based on experimental data collected with the exoskeleton. The results show that the proposed model better captures the non-linear behaviour of the exoskeleton's actuation system, increasing overall descriptive performance by 15%. However, adding the adhesion offset to extend the relation of static friction, does not improve the model.

1. Introduction

Assistive robot technologies, such as exoskeletons, help users with everyday tasks or augment their capabilities. These are the goals that drive the exoskeleton research. Several reviews explain the scope of research and the progress of the proposed devices, e.g. exoskeletons of the lower extremities [1], exoskeletons of the upper extremities [2], exoskeletons for the rehabilitation [3], design, history and control aspects of exoskeletons [4], etc. Some devices have already been developed to the point where they are available to end-users; however, these essentially still offer limited performance and power capacity and are expensive [3].

A large part of state-of-the-art exoskeletons aims at slow tasks, such as standing, walking on level ground, climbing stairs, sitting or standing up. Challenges to achieve a good performance in such tasks include human-machine interaction, adaptation to user variability, sensor integration, actuator design, appropriate control strategies, and others, all of which are still being pursued [2]. A major limiting factor for highly dynamical tasks, such as running, jumping, throwing, hammering, etc., is the mass of robots, robot arms, and exoskeleton frames [5].

With the addition of batteries and motors, the mass of an exoskeleton device increases rapidly. This increased robot arm mass negatively impacts safety [6]. Increased safety is the reason for the transition from heavy industrial robots to robots with lighter arms,

* Corresponding author.

E-mail address: miha.dezman@kit.edu (M. Dežman).

URL: <https://www.mihadezman.com> (M. Dežman).



Fig. 1. Exoskeleton prototype in use.

which allow safe and close human–robot collaboration [5]. Additionally, research shows that excessive mass of wearable devices negatively affects the energetics of human movement and increases metabolic costs [7]. Lighter robot arms or frames feature smaller inertias, thus allowing for more dynamic tasks [8,9]. Thus weight minimization is a vital exoskeleton design goal.

A direct way to minimize the exoskeleton frame's mass and inertia is to remove the heavy components, e.g. motors, gears, etc., from the frame and place them closer to the user's centre of mass [10,11]. The forces and torques are transmitted from the motor over a distance to the exoskeleton joint using mechanical power transmission. *Bowden cables* represent one of such mechanical power transmission technologies for remote actuation [12,13]. A number of papers report their use [14–17] and evaluate their reliability [18]. Bowden cables' main advantages are their compactness and mechanical design flexibility, which enable lightweight mechanical designs [19] as the cables can be routed and bent around the frame and joints of the exoskeleton. Additionally, springs allow adapting their passive behaviour in a compact manner [20].

Soft exosuits represent a successful application of the above-mentioned mass and inertia minimization principle, which results in some of the lightest exoskeleton devices [10,21–23]. Fabric and garnets replace the metal frames, and the actuation units are placed away from the user's limbs, and Bowden cables transfer the power for assistance [24]. As the fabric garments are lightweight, highly dynamic tasks like running [22] are possible. However, the strength of fabric limits the maximum assisting forces, which are much lower than those of rigid exoskeleton frames [25].

Bowden cable transmission design advantages are apparent, but the inherent friction and other non-linearities along the cable transmission worsen the control performance if they are not adequately compensated for [26,27]. Adverse effects include static and dynamic friction phenomena between the cables and Bowden sheaths, with backlash and hysteresis related to the bending angle [19]. Furthermore, cable preload is another parameter that results in higher friction since it increases the normal forces in the system [27].

Friction compensation, or more precisely non-linearities compensation, should therefore be applied when Bowden cables are used [28]. For a successful compensation of bending related friction, its variability needs to be mechanically reduced or identified with additional sensors. As a mechanical solution, root looping shows good results [26], since it decreases the effect of bending although at the cost of higher friction. Another mechanical method to reduce the effect of bending on friction is with the addition of redirection pulleys [29]. The downside here is a higher mechanical complexity; however, the overall friction is lower since small pulleys redirect cable routing and replace Bowden sheath bending. Alternatively, additional sensors and redundant sensor architectures allow backlash compensation and accurate torque control [30]. However, as a drawback, any potential tension change or cable creep requires a new system calibration. Furthermore, the friction amounts remain the same. Bending sensing is another way to improve the control performance, for example, with an embedded auxiliary wire that senses the bending [31,32].

Finally, the elastic deformation of the Bowden cable is another non-linearity. It is the summation of the steel cable stretching, Bowden sheath compression and potential elastic deformation of other structural components [30,33]. This elastic deformation effect indicates the external load on the actuator and is suitable for use in control [33–35].

The complete removal of rigid frames is not the only way to build efficient exoskeletons. The passive overhead work assistance exoskeletons are an excellent example of recently developed passive exoskeletons [36]. The frame's additional passive degrees of motion ensures kinematic compatibility with a user's biomechanical structure. Nonetheless, while the application of these exoskeletons is only limited to the arm support for work above the head, additional actuated degrees of motion could improve their functionality and range of applications. Furthermore, the frame could remain lightweight using Bowden transmission technologies for remote actuation.

Our research group is developing a prototype exoskeleton to assist the motion of the upper extremities in such a manner. Fig. 1 shows the actual prototype in use. The design of passive exoskeletons for overhead work tasks [36] inspired the exoskeleton's kinematic structure. Our prototype uses two active degrees of motion to extend its functionality above a passive exoskeleton's functionality.

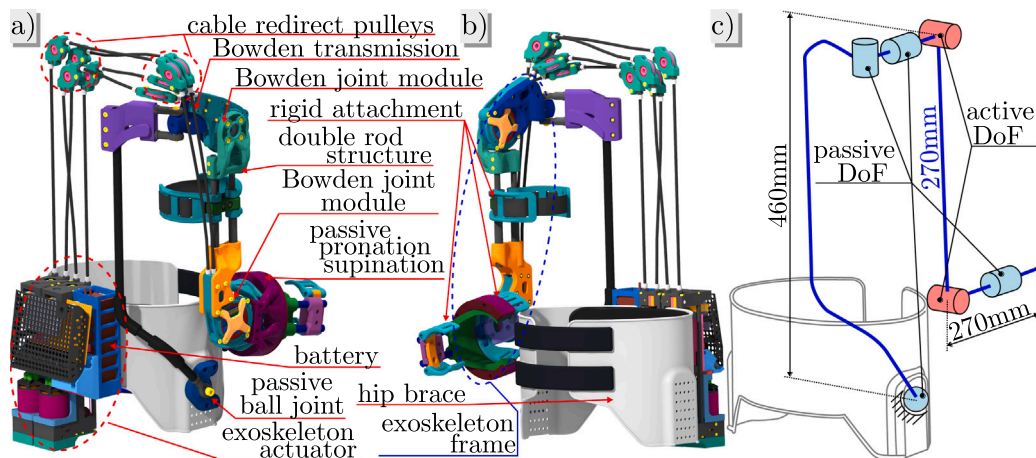


Fig. 2. Two views of the virtual exoskeleton prototype in (a) and (b). Its most important components are marked. (c) shows the kinematic structure of the exoskeleton. The two actuated degrees of freedom are coloured red, and the passive degrees of freedom are in light blue. The figure also indicated some rough exoskeleton dimensions. (For interpretation of the references to colour in this figure legend, the reader is referred to the web version of this article.)

1.1. Contributions

The first contribution of this paper is a set of mechanical solutions based on Bowden cable technology needed to achieve the necessary torque requirements of activities of daily living (ADL) at the shoulder and elbow joints. A vital aspect addressed in this paper is the design and evaluation of the underlying actuator and transmission technology, critical for lightweight, low-inertia exoskeleton frames. The paper also presents other mechanical solutions, e.g. an integrated load-cell for bidirectional measurements of Bowden cable forces and redundant encoder structures to measure the elastic deformations of Bowden cables. However, the paper does not evaluate the performance of these two sensors.

A new actuator model that relies on a modified underlying friction model is the second contribution of this paper. The model is used to identify the unknown electrical motor and friction model parameters of the proposed actuation unit. The friction model is based on an adhesion offset-based Coulomb friction component and is the main novelty of this work. The offset improves the model's capability to capture the system non-linearities of the proposed exoskeleton system. Additionally, the effect of the adhesion parameter is also added to the static friction component of the Coulomb-Friction model and evaluated. Otherwise, such offset modelling plays a vital role in the modelling of mechanics of granular media and soils account for adhesive contributions between particles [37]. However, in the modelling of exoskeleton cable transmission, the adhesive behaviour between the Bowden cable and Bowden sheath is often neglected and not researched [26,32,38,39]. Currently, the proposed actuator model considers only the effects of motor velocity and external load on friction. This paper does not explore the effects of bending and preload on cable friction but establishes the theoretical foundations needed to investigate their impact in future work.

The paper is structured as follows: Section 2 forms the first part of this work and focuses on the mechanical solutions of the proposed exoskeleton device, its actuation unit and the underlying electronics and control. Section 3 starts the second part of this work and presents the mathematical modelling of the actuator system and the novel friction model. Finally, Section 4 presents and discusses the experimental system and evaluation results of the proposed actuator model on the data gathered from the actual exoskeleton system. This part serves both to show the performance of the exoskeleton device from the first part and the performance of the proposed actuator model. Lastly, Section 5 concludes the paper.

2. Upper-limb exoskeleton design

The proposed exoskeleton's mechanical structure features a lightweight frame with manual adjustment to different user shapes. Fig. 2a,b show the exoskeleton from two different angles and list its main features. Fig. 2c shows the kinematic structure of the exoskeleton.

2.1. Exoskeleton design

The current design of the exoskeleton augments the shoulder's vertical flexion/extension and flexion/extension of the elbow. See the two red coloured active rotational joints in Fig. 2c. Their selection represents a compromise between the desired support for the human arm and the exoskeleton mechatronic complexity. They enable gravity compensation of the user's upper and lower arm sections. Several additional passive rotation degrees of motion allow for kinematic compatibility with the user and unhindered motion. The passive rotational joints are coloured light blue in Fig. 2c. The lightweight frame structure is made possible by moving the exoskeleton motors to the user's back and combining 3D additive technology and aluminium components. The aluminium

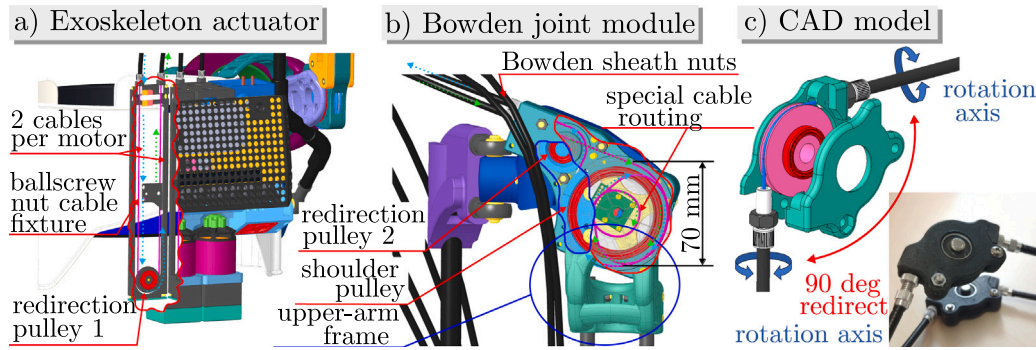


Fig. 3. Bowden cable transmission and Bowden joint module. (a) depicts cable routing on the actuator; (b) depicts cable routing on the Bowden cable joint module. Cable routing direction is indicated by *blue* and *green* arrows. (c) depicts the **redirection pulleys** that are placed along the Bowden cable sheath to redirect the cable and reduce the total cable bend. (For interpretation of the references to colour in this figure legend, the reader is referred to the web version of this article.)

components are manufactured using traditional methods, while the rapid prototyping technology uses additive manufacturing of fibreglass-reinforced plastic. Including the battery, the final exoskeleton weighs 7.7 kg, while the whole arm frame structure weighs only 1.7 kg.

A Bowden cable transmission transmits the mechanical power of the motors to the exoskeleton frame. The exoskeleton actuation unit is attached to the backside of the hip orthosis. The frame is attached to the side of a *hip orthosis* via a passive ball joint, see Fig. 2. This ball joint transfers the loads from the frame onto the hip orthosis and the user's hip. Therefore, the hips carry the exoskeleton device.

Fig. 2a,b shows two Bowden joint modules and interconnecting links. All Bowden joint modules have the same design, which reduces the variability of exoskeleton components. The Bowden cables separate the exoskeleton actuator from the frame structure, enabling different designs or redesigns of the frame, thus allowing for modularization. The exoskeleton actuator's mass does not affect the ergonomic and carrying characteristics of the frame, allowing the user to move freely because the actuation units are located away from the end-effector. Since the actuator components such as motors, power electronics and batteries are localized, electrical cables and the cooling design are simplified, resulting in a compact and power-dense actuator unit.

Fig. 3 shows details of the Bowden cable transmission as realized on the actuator side (Fig. 3a) and on the Bowden joint side (Fig. 3b). The cable is continuously routed from the actuator unit, to and through the Bowden joint and back to the actuator unit. The cable ends rigidly connect to the ball screw nut at the actuator. In the Bowden joint module, the cable is guided through the middle of the pulley to form a loop, observed in Fig. 3b. The loop increases cable friction and prevents slippage on the pulley. The cable then runs around the *redirection pulley 2*, which brings the two Bowden cable nuts closer together, creating a compact Bowden connection module. The cable ends again at the actuator through the second Bowden cable sheath. It moves along the actuator's length and is guided around the deflection pulley 1 to finally end at the ball screw nut, where it is rigidly connected and where both cables ends meet.

Note that while the cable is routed continuously through the Bowden joint pulley, each Bowden joint cannot rotate continuously but allows for a limited rotation of 270 deg. However, this is an acceptable rotation range for assistance at the targeted human elbow, and shoulder joints [40]. Additionally, two pairs of redirection pulleys are added along each Bowden sheath, see Fig. 3. The isolated pulleys are shown in Fig. 3c. These additional pulleys allow easier routing and movement of Bowden sheaths along with the exoskeleton frame. Using them, the exoskeleton frame's movement at the shoulder and elbow joints reduces the bending of the Bowden cable transmission lines. Such pulleys also reduce the overall friction in a Bowden cable [29]. The Bowden cable sections remain straight, while the redirection pulleys provide a 90°(one pulley) or a 180°(two pulleys) bend. Fibreglass reinforced plastic is combined with aluminium to construct these pulleys, weighing around 40 g. A Bowden sheath of a thickness of 5 mm is stiff enough to remain upright despite the combined weight of the Bowden cable and redirection pulleys.

2.2. Actuation unit

The actuation unit combines a brushless motor with a ball-screw and timing belt pulley transmission. Two sectional views in Fig. 4 show its inner workings. The two views depict the location of the motors and the timing belt transmission between the electric motor and the ball-screw in Fig. 4a. One can also see the ballscrew nut and its cable fixture in Fig. 4b. The timing belt protects the motor from vibration and allows small manual adjustments towards the final transmission ratio by replacing the timing belt pulleys with different teeth numbers. The ball-screw is difficult to back-drive, requiring less torque to maintain a given position under load. It also allows for straightforward linear motion of the attached cable.

Fig. 4b also shows the integrated load-cell and its lever mechanism that allows for bidirectional force measurements in both respective cable sheaths. This integrated load cell sensor directly measures the Bowden cable's loads by measuring the forces on the ball-screw. A lever arm is used to integrate the load cell into the system, as seen in Fig. 4a and b. Therefore, the load cell signal

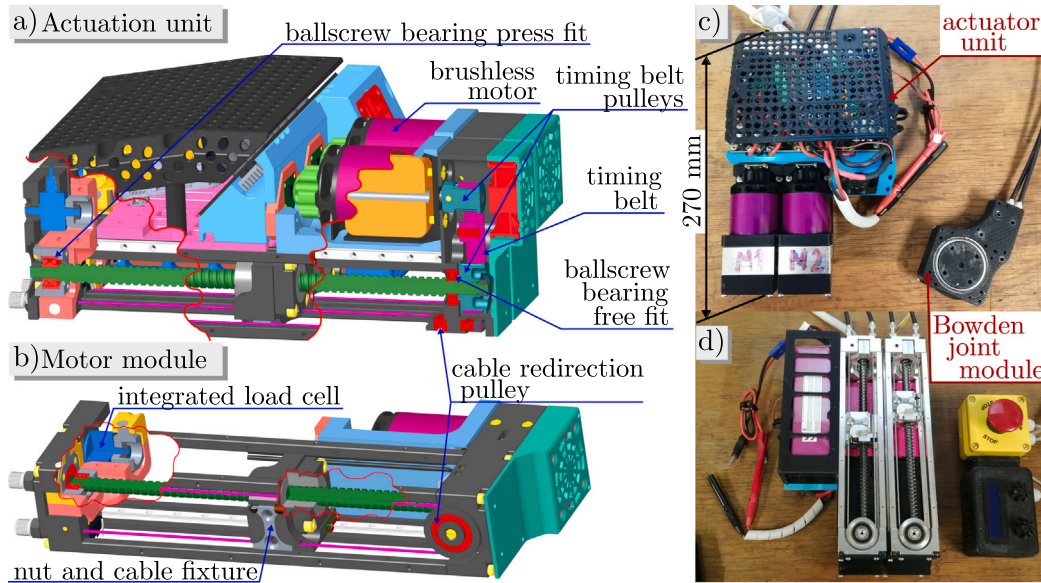


Fig. 4. Actuation unit of the exoskeleton. Two section cuts expose its inner workings as shown in (a). The motor module with its ballscrew transmission and two section cuts is shown in (b), which also shows the integrated load cell and the mechanism that prevents torque loads on the load cell. (c) and (d) show the actuator unit prototype and the Bowden joint module from different views.

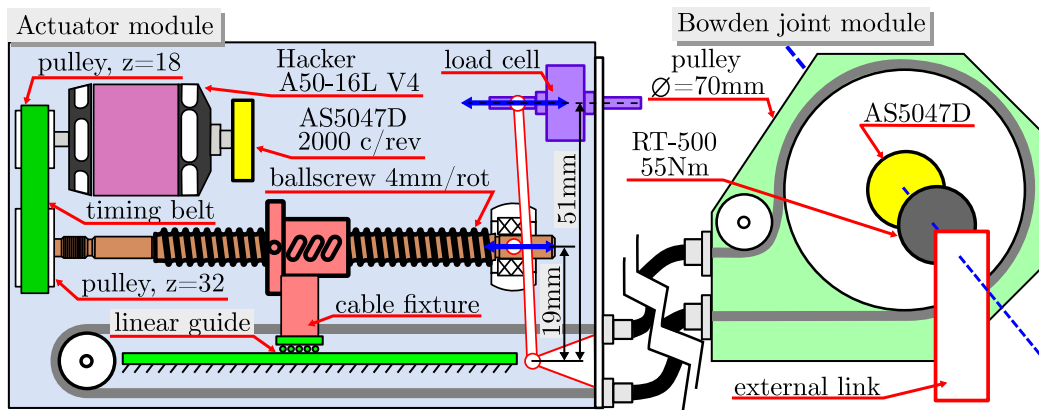


Fig. 5. A schematic representation of the mechanical system. The schematic shows different components and a simplified insight into sensor placement, load cell integration and operation of the actuator transmission system.

registers the tension loads of both cable ends and displays them as positive and negative voltage. The load cell is a consumer product (500N DCE, LCM Systems Ltd.). The exoskeleton joint features another torque sensor (RT-500, 55 N m, Tovey Engineering) that allows for experimental evaluation and validation of other sensors. However, in the final exoskeleton this sensor will be removed and the exoskeleton prototype will function without it. Fig. 4c,d shows the built actuator prototype.

Fig. 5 shows a schematic representation of the architecture. A brushless out-runner motor Hacker A50-16L V4 serves as the main drive. The selected motor can reach a temporary maximum output power of 1650 W for 15 s, much more than required for the selected application. Its torque constant, required for torque based control design, is not specified in its accompanying documentation. As the actual exoskeleton requirements are unknown, partly due to the unknown level of cable friction and the fan cooling effectiveness, a more powerful motor was chosen to provide an operational margin. The timing belt transmits the rotation from the motor to the rotation of the ball-screw, which in turn moves the ball-screw nut linearly. Turning the ball screw clockwise or counterclockwise moves the nut forward or backwards. The nut is attached to a small linear guide improving the nut's resistance to non-axial forces and torques. Moreover, the Bowden cable rigidly connects to the nut meaning that bidirectional linear movement of the ball screw nut rotates the Bowden joint.

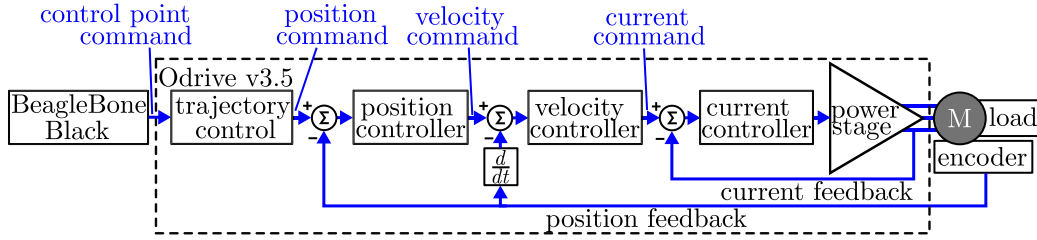


Fig. 6. Upper-limb exoskeleton position controller. The schematic shows the proposed system's position controller built by combining the Odrive position control mode and the trajectory mode. The diagram is partly adapted from Odrive manual (ODrive Robotics, Richmond, CA).

The combined mechanical transmission ratio of the system is:

$$n_m = 70\pi \frac{\text{mm}}{\text{rot}} \cdot \frac{1}{4} \frac{\text{rot}}{\text{mm}} \cdot \frac{32}{18} = 97.74 \quad (1)$$

Here, $70\pi \frac{\text{mm}}{\text{rot}}$ is the circumference of the Bowden joint pulley and represents the length of cable needed to rotate the pulley for one rotation. The $\frac{1}{4} \frac{\text{rot}}{\text{mm}}$ and $\frac{32}{18}$ are the transmission of the ball screw and the timing belt, respectively.

As shown in Fig. 5, each motor uses two AS5047D (ams AG, Austria) encoder sensors. The first is integrated into the Bowden joint module to provide an absolute measurement of the external link position. The second AS5047D encoder is placed on the motor axis and operates in the incremental signal mode for motor driver position feedback.

2.3. Electronics and control design

A combination of several community-supported development platforms forms the electronics of the exoskeleton system. BeagleBone Black (BBB) is the primary control board that runs the exoskeleton control algorithm. The BBB runs under an open-source Linux distribution and thus supports custom software development. An additional microcontroller, called Teensy LC, is used to reduce the load on the BBB. Finally, a brushless open source and open hardware motor driver, called Odrive v3.5, is used (ODrive Robotics, Richmond, CA). While BBB allows using different programming languages, Python is the primary programming language in this work. Finally, BBB has a built-in wireless network adapter that allows wireless communication to provide user input or data streaming.

The **Position Controller** relies on the control algorithm shown in Fig. 6 to control the motors in position mode. Both the position-based and the current-based motor controls are possible on the Odrive. In this implementation, the BBB sends trajectory control points at a frequency of 50 Hz to the *Trajectory Controller* of the Odrive. The Odrive interpolates them with a trapezoidal velocity profile running at a higher control frequency. The proposed controller allows a stable exoskeleton operation despite the low-frequency limitation of the UART communication's protocol currently implemented. A faster communication protocol would allow a higher control loop frequency. The position controller does not consider the cable elongation or other elastic deformations of the system. All control point commands are therefore sent in a feedforward manner.

3. Actuator and friction modelling

3.1. Actuator model

A standard electric motor torque equation establishes the **basic actuator model**. Based on [41], the following equation holds to achieve a static equilibrium between the motor torque, external load and friction.

$$\tau_m \rightarrow I_m \cdot k_a = \tau_{\text{ext}} + \tau_{\text{fr}}, \quad (2)$$

where τ_m is the motor torque calculated as a product between the motor current I_m and the actuator torque constant k_a . This motor torque is the sum of the external torque τ_{ext} and non-linear term τ_{fr} . The non-linear term τ_{fr} depends on friction, hysteresis, static friction, dynamic friction, and other dissipation effects accumulated along the Bowden cable transmission. The actuator torque constant k_a captures the linear relation of the motor current and its armature torque, and the combined mechanical transmission of the actuation system.

Because the friction in such Bowden cable transmission system is large [42], the non-linear τ_{fr} component has a big effect on how well the above Eq. (2) describes the actual actuation system. Therefore, the descriptive power of the friction model is important and narrates the quality of the actuator model. The Stribeck+ Coulomb model τ_{SCM} is used to describe the non-linear term τ_{fr} in this work, because it is an established approach to friction modelling [43]. This friction approximation forms the **underlying friction model** of the above basic actuator model. Other model also exist for example LuGree friction model [43,44]. Although these models describe additional non-linear behaviours, they also rely on mathematical models of higher complexity and are for this reason not evaluated at this stage of research. The Stribeck+ Coulomb model is a friction model with reasonable mathematical complexity that will allow future model extension with additional custom parameters to describe nonlinearities in the proposed exoskeleton system.

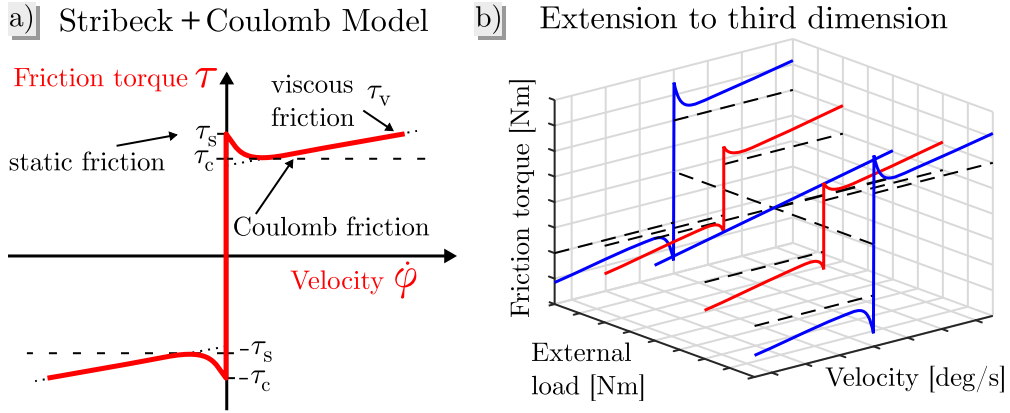


Fig. 7. Stribeck+ Coulomb friction model. (a) shows the friction force as a function of velocity. The complete friction model is composed of static (τ_s), Coulomb (τ_c) and viscous friction (τ_v). (b) shows the expansion of the model towards the third dimension.

If the unknown parameters of the Stribeck+ Coulomb model τ_{SCm} and the actuator torque constant k_a are identified, the Eq. (2) allows for inverse calculation of the actuator current. From the control point of view, the external torque becomes the desired control torque ($\tau_{ext} = \tau_{des}$), thus Eq. (2) converts into:

$$I_m \approx \frac{\tau_{des} + \tau_{fr}}{k_a}, \quad \text{where} \quad \tau_{fr} = \tau_{SCm}(\tau_{des}, \dot{\varphi}_m). \quad (3)$$

This equation forms the proposed **actuator model** of this work. It calculates the required current I_m to exert a desired torque τ_{des} at the exoskeleton joint in relation to the motor velocity $\dot{\varphi}_m$ and the desired torque τ_{des} .

3.2. Classic Stribeck + Coulomb Friction Model

The Classic Stribeck + Coulomb model follows the equation:

$$\tau_{SCm}(\tau_{ext}, \dot{\varphi}_m) = \left[\tau_c(\tau_{ext}) + \dots \left(\tau_s(\tau_{ext}) - \tau_c(\tau_{ext}) \right) \exp^{-|\dot{\varphi}_m/v_s|^{\delta_{SCm}}} \right] \text{sign}(\dot{\varphi}_m) + k_v \dot{\varphi}_m. \quad (4)$$

It consists of three types of friction: static friction τ_s , Coulomb friction τ_c and viscous friction $\tau_v = k_v \dot{\varphi}_m$. See an example friction curve with the important friction model components in Fig. 7. The other two parameters δ_{SCm} and v_s exponentially decrease the effect of the static friction τ_s in the above equation.

The Stribeck + Coulomb model depends additionally on motor velocity $\dot{\varphi}_m$ and external load τ_{ext} . The motor velocity $\dot{\varphi}_m$ determines the direction Coulomb friction τ_c and the direction and the magnitude of attenuation of static friction τ_s . Additionally, the velocity also affects the viscous friction component. See the effect of velocity on friction in Fig. 7a. To show the effect of τ_{ext} on the friction curves, Fig. 7a needs to be extended to the third dimension, as shown in Fig. 7b.

Typically, the Coulomb friction force F_c is defined to have the following linear relation with normal force F_n [45], i.e. the third dimension of Fig. 7b:

$$F_c \leq n_c F_n. \quad (5)$$

This friction behaviour is well researched and analysed in the literature in systems with lesser amounts of friction [44]. Note that the referenced work [45] examines linear friction forces and components (F_c, F_n), however this work considers their rotational equivalents (τ_c, τ_n). Alternatively, Eq. (5) can also be extended with an offset to represent adhesion phenomena:

$$F_c = F_0 + n_c F_n. \quad (6)$$

Eq. (6) is typically used in the modelling of mechanics of granular media and soils account for adhesive contributions between particles [37]. However, the adhesive behaviour in the Bowden cable system is often neglected and not researched in the exoskeleton field [26,32,38,39].

Note that in the present Bowden cable system, the external load τ_{ext} has a similar effect as the normal force F_n , since with the external load increase, the forces in the transmission cable, on the pulleys, on the ball screw, on bearings and on the belt transmission all increase. Therefore, the τ_c dependence on τ_{ext} from Eq. (4) is defined as:

$$\tau_c(\tau_{ext}) = n_c \text{abs}(\tau_{ext}). \quad (7)$$

And the same logic applies to the static friction τ_s relation:

$$\tau_s(\tau_{\text{ext}}) = n_s \text{abs}(\tau_{\text{ext}}). \quad (8)$$

The parameters n_c and n_s are the two constants that establish a linear relation between friction and τ_{ext} . Eqs. (7) and (8) thus form the basis for the Coulomb and static friction calculations in the **Classic Stribeck + Coulomb model**. In both Eqs. (7) and (8), the absolute value of τ_{ext} is taken, since the τ_{ext} torque can be both negative and positive, which is not true for the normal force F_n from Eq. (5).

3.3. Modification of coulomb and static friction

This work modifies the Coulomb friction component τ_c with an offset to model adhesion behaviour. Such principle is often used in the modelling of soil mechanics [37]. This modification improves the model's descriptive capability of the proposed exoskeleton system's nonlinear behaviour.

First, a **Variant A friction model** $\tau_{\text{SCm,A}}$ is created that relies on the classic friction model τ_{SCm} from Eq. (4), but redefines its Coulomb friction relation from Eq. (7) to equation:

$$\tau_{\text{mc}}(\tau_{\text{ext}}) = n_{c1} \text{abs}(\tau_{\text{ext}}) + n_{c2}. \quad (9)$$

Here, an additional constant n_{c2} is introduced and the original constant n_c from Eq. (7) is renamed to n_{c1} . This offset parameter n_{c2} tries to address the fact that even when the system is not loaded, there is still some Coulomb friction and static friction to be overcome due to the system's preload. The Variant A underlying friction model equation is thus:

$$\tau_{\text{SCm,A}}(\tau_{\text{ext}}, \dot{\varphi}_m) = \left[\tau_{\text{mc}}(\tau_{\text{ext}}) + \dots \left(\tau_s(\tau_{\text{ext}}) - \tau_{\text{mc}}(\tau_{\text{ext}}) \right) \exp^{-|\dot{\varphi}_m/v_s|^{\delta_{\text{SCm}}}} \right] \text{sign}(\dot{\varphi}_m) + k_v \dot{\varphi}_m. \quad (10)$$

Note that the description of static friction τ_s remains the same as in the classic friction model from Eq. (7).

Second, a **Variant B friction model** $\tau_{\text{SCm,B}}$ is created on the same principle, but extends the static friction τ_s description by prescribing an offset to Eq. (8):

$$\tau_{\text{ms}} = n_{s1} \text{abs}(\tau_{\text{ext}}) + n_{s2}. \quad (11)$$

The Variant B friction model relies both on Eqs. (9) and (11) and evaluates if the addition of the offset on static friction component improves the descriptive capability of the friction model. The full friction model in this case is:

$$\tau_{\text{SCm,B}}(\tau_{\text{ext}}, \dot{\varphi}_m) = \left[\tau_{\text{mc}}(\tau_{\text{ext}}) + \dots \left(\tau_{\text{ms}}(\tau_{\text{ext}}) - \tau_{\text{mc}}(\tau_{\text{ext}}) \right) \exp^{-|\dot{\varphi}_m/v_s|^{\delta_{\text{SCm}}}} \right] \text{sign}(\dot{\varphi}_m) + k_v \dot{\varphi}_m. \quad (12)$$

It is important to note that this work does not explore the effects of bending and preload. While the literature describes the effect and importance of these two properties [46], the goal of this work is to establish the theoretical foundations for future the exploration of these effects on the proposed exoskeleton system.

4. Experimental evaluation and discussion

The actuator model from Eq. (3) is used in combination with one of the three friction model's to identify the parameters of the exoskeleton joint. To briefly summarize, the three friction models are:

- the **Classic model**, where Coulomb friction features a linear relation to normal force without offset.
- the **Variant A**, where an additional offset is proposed to the linear relation between Coulomb friction and normal force to improve its descriptive capability.
- the **Variant B** explores whether the model improves if the same offset concept is applied both to the Coulomb friction and to the static friction.

The exoskeleton's shoulder joint data is used to evaluate the modelling capabilities of the proposed friction model variants. More specifically, the model should represent the relation between motor current, external load and motor velocity.

For evaluation, the underlying model parameters are optimized to provide the best fit to the measured data. A better friction model fits closer to the measured data and provides a better representation of the actual system. This in turn enhances the motor current prediction from Eq. (3). The mean squared error (MSE) represents the difference between the actual motor current and the theoretical current calculated via the actuator model, where the model relies on one of the three different friction models. Later, the MSE values are compared between the three friction model's and discussed.

Both the unknown actuator torque constant k_a and the parameters of the respective friction model (τ_{SCm} , $\tau_{\text{SCm,A}}$, $\tau_{\text{SCm,B}}$) are optimized in one experiment per friction model. Note that alternatively, a separate experiment could identify the actuator torque constant k_a , since the constant depends on the electric motor torque constant and the transmission of the mechanical system. However, the friction measurement experiment procedure would remain the same despite that. Therefore, performing two experiments would only decrease the straightforwardness of the current experimental procedure.

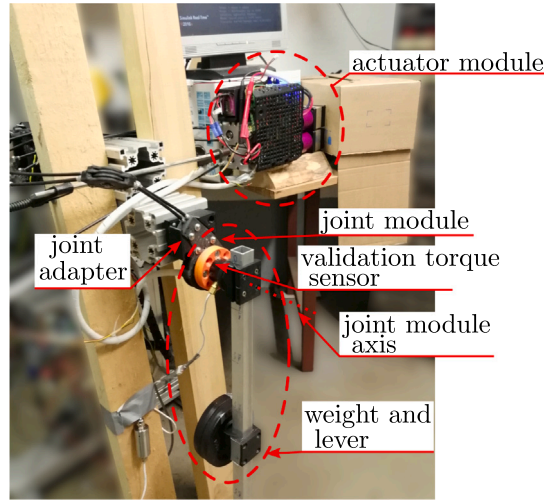


Fig. 8. Experimental system. The Bowden joint module was removed from the exoskeleton's frame and mounted on an aluminium stand. An additional torque sensor connects the lever and the weight to the exoskeleton joint.

4.1. Experimental system and experimental data

The exoskeleton's shoulder joint was detached and mounted on an aluminium stand to construct the experimental system. The joint's preload was adjusted by screwing the Bowden cable screws until there was no noticeable slack. For the remainder of the experiment, the preload was not further adjusted. To minimize the effect of the cable bending, the location of the exoskeleton joint to the actuator module remained the same. Note that this paper does not evaluate the effect of cable bending and preload on the proposed model but establishes a basic theoretical actuator model to allow future research of these effects.

An additional validation torque sensor connects the exoskeleton joint and the lever. The lever allows the attachment of different weights at different lengths to simulate external loads on the actuator. Furthermore, swinging the weights at different velocities represents most of the torque velocity measurement points. Fig. 8 shows the experimental system used to collect the necessary data to construct the mathematical models of friction.

Throughout the experiments, a position controller regulates the motors in a way to overcome any friction, see Section 2.3. An external torque sensor stands between the joint and the lever and measures the desired (external) torque τ_{des} generated by the motion of the lever and the weight on the joint. The data is collected in several measurement sessions to determine the properties of the Bowden cable-based actuator reliably. Fig. 9a,b,c show a 700 s long section of measurement data that were obtained in a 4958 s long measurement session. Data is sampled with a frequency of 50 Hz. The full 4958 s signal consists of sinusoidal signals with different offsets and different loads. To better capture the non-linear friction zero-velocity transitions, step signals were also performed at different loads and offsets, as seen in Fig. 9a between the time window of 500 s and 700 s. Fig. 9d shows all the measured points in a 3D visualization and illustrates the relationship between the motor current, external torque and motor velocity.

At this stage, the data gathered in Fig. 9d shows that the proposed actuation generates a torque spanning from about -20 N m to 20 N m, seeing the external torque axis. Similarly, the velocity spans from roughly -140 deg/s to 140 deg/s, as shown in the velocity axis. Note that external load torque is equal in magnitude to the torque exerted by the exoskeleton joint.

The non-linear motor current transition along the zero velocity axis shows friction as the system changes the movement direction. It is easily noticeable (see the big step jump along the zero velocity axis), and the shape of the diagram is similar to the proposed friction model in Fig. 7b. Note that the z axis in Fig. 9d does not depict the friction directly but shows the motor current required to produce the equivalent motor torque equal to the desired (external) torque and the additional torque needed to overcome the friction.

4.2. Optimization process

The unknown parameters are the actuator torque constant k_a and the friction curve parameters of the respective underlying friction models (τ_{SCm} , $\tau_{SCm,A}$, $\tau_{SCm,B}$). Here are the parameter vectors that need to be optimized to fit the data for each of the respective actuator model and friction model combination:

$$\mathbf{x}_{SCm} = [n_c, k_v, n_s, v_s, \delta_{SCm}, k_a], \quad (13)$$

$$\mathbf{x}_{SCm,A} = [n_{c1}, n_{c2}, k_v, n_s, v_s, \delta_{SCm}, k_a], \quad (14)$$

$$\mathbf{x}_{SCm,B} = [n_{c1}, n_{c2}, k_v, n_{s1}, n_{s2}, v_s, \delta_{SCm}, k_a]. \quad (15)$$

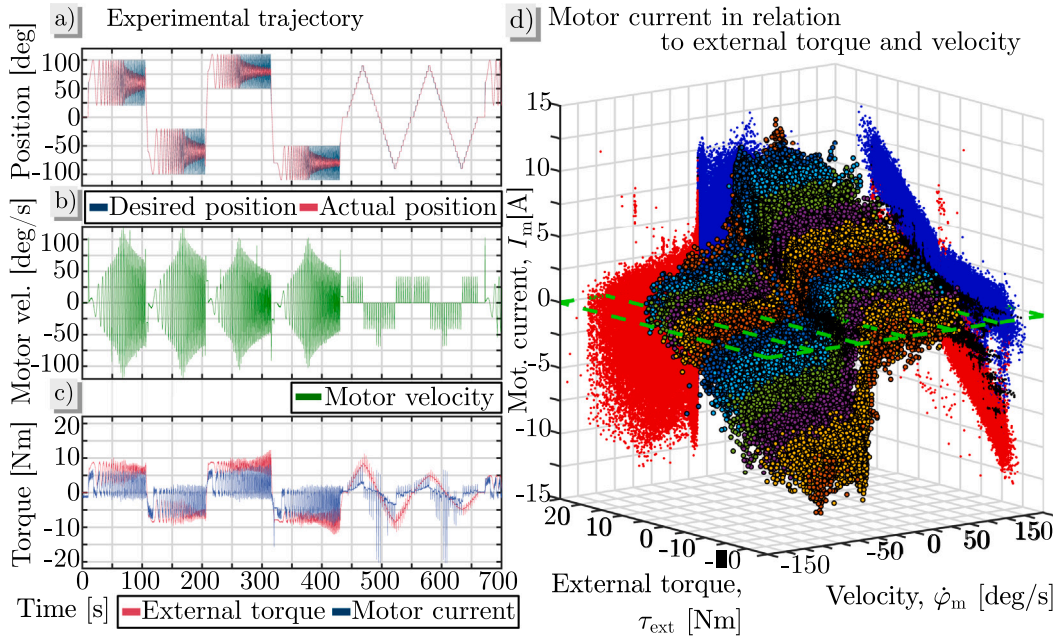


Fig. 9. Experimental data plot. The desired and actual motor trajectory are shown in (a), motor velocity in (b), and motor current and external torque in (c). Only the first 700 s are shown out of 4958 s. (d) shows another visualization of measurement points. The measurement points are coloured in segments along the external torque axis. *green* dashed lines improve data visibility. The measurement points are also projected onto the planes behind the graphs in *red* colour for negative velocity, *blue* colour for positive velocity, and *black* colour for zero velocity. (For interpretation of the references to colour in this figure legend, the reader is referred to the web version of this article.)

Table 1
ADL requirements.

Movement	ROM [°]	Vel. [°/s]	Acc. [°/s ²]	Torque [N m]	Power ^a [W]	Source
Shoulder flexion/extension	100 to -135	71	103	20	24.8	[40]
Elbow flexion/extension	0 to 135	91	116	20	31.8	[40]

^aPower calculated as the multiplication of the respective row's velocity value and torque value.

The constrained optimization function *fmincon* from Matlab[®] with multi-start property is used to find the global solution of the above parameters. All the parameters are constrained to remain positive and non-zero. The following *cost* function is to be minimized:

$$cost = \text{MSE} \left(I_m, \frac{\tau_{\text{ext}} + \tau_{\text{fr}}}{k_a} \right), \quad (16)$$

where τ_{fr} is replaced with the respective friction model. The actuator model with the respective underlying friction models best fits the data when the mean-squared error reaches the minimum value.

4.3. Results: ADL requirements

The activities of daily living (ADL) determine the exoskeleton joint's maximum torque and velocity requirements. Table 1 gathers the ADL requirements from [40] for the elbow flexion/extension and shoulder flexion and extension. According to [40], the maximum required velocity and torque of the shoulder joint is roughly 71 deg/s and 20 N m, respectively. However, the elbow joint has a higher maximum velocity of roughly 91 deg/s but the same amount of maximum torque (20 N m).

Fig. 10a depicts the values from Table 1 and the data sparsity of measurements from Fig. 9d. The sparsity plot shows how often the required torque and velocity combination were measured. Note that the colours represent a logarithmic scale. The number of samples representing a specific torque/velocity combination is counted on a small grid. This grid is represented with small dots in Fig. 10a. The colour represents the number of samples nearest to a specific grid point. Note that the colour change represents a logarithmic increase.

As depicted, the exoskeleton meets the ADL requirements from [40], i.e., a maximum velocity of 71 deg/s and a maximum torque of 20 N m for the shoulder joint. It also fulfils the elbow joint requirements, i.e., it reaches a maximum velocity of 91 deg/s and a maximum torque of 20 N m.

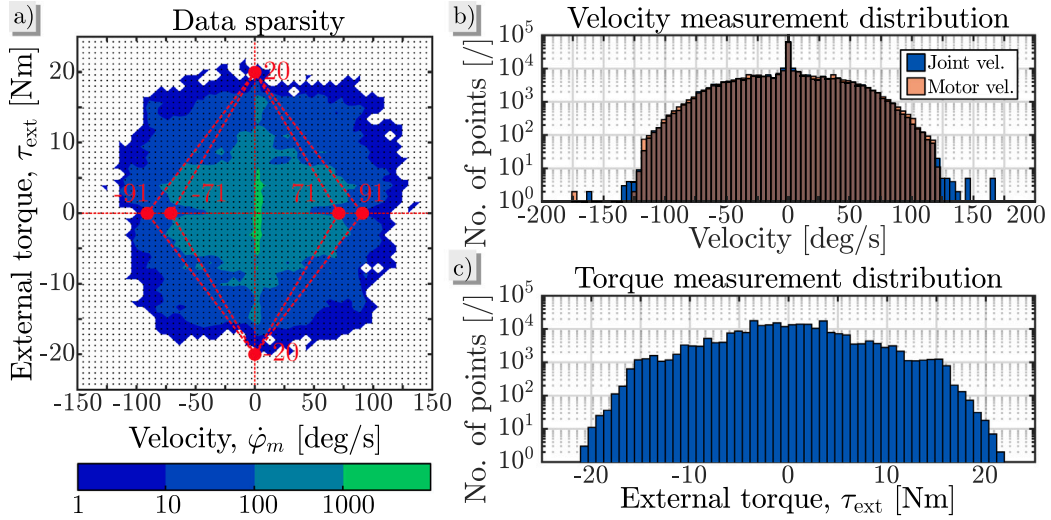


Fig. 10. Data sparsity of measurements. (a) shows the number of measurement points in the velocity/torque space. The number of samples representing a specific torque/velocity combination is counted on a small grid. The logarithmically increasing colour shows the number of measurement samples closest to a specific vertex of the counting grid. (b) shows the histogram distribution of the measurement points for the velocity at the motor and the joint end. Finally, (c) shows histogram distribution for the external torque measurements. (For interpretation of the references to colour in this figure legend, the reader is referred to the web version of this article.)

Table 2
Results.

Model	Par. no.	MSE	Impr. ^a [%]
Classic model	6	0.8966	/
Variant A	7	0.7624	14.97
Variant B	8	0.7622	14.99

^aImprovement column depicts the percentage difference between the Classical model MSE and the respective Variant A or B.

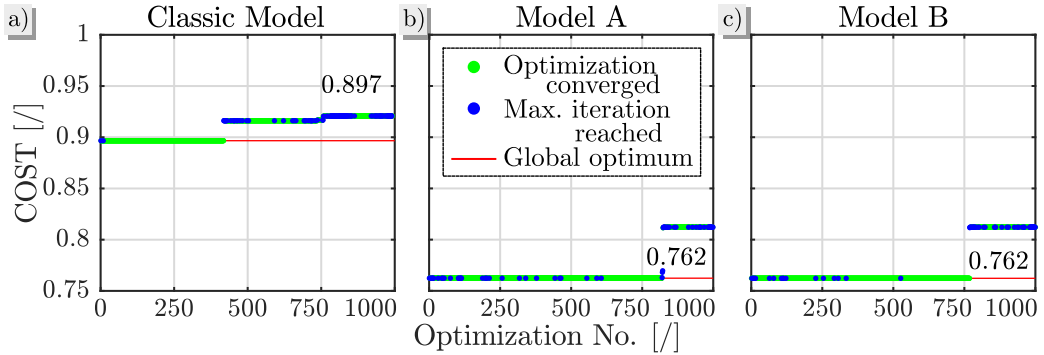


Fig. 11. Solution robustness. COST values of 1000 additional local constrained optimizations are shown in (a), (b) and (c), for the Classic model Variant, Variant A and Variant B, respectively.

4.4. Results: Friction modelling

Table 2 gathers the resulting mean-squared values. Observe how both friction variants improve the actuator model fit to the measured data, i.e., feature a lower MSE value than the classic Stribeck + Coulomb friction model. Variant A with the offset Coulomb friction relation achieves an MSE value of 0.7624, i.e., roughly 15% lower than the MSE value of 0.8966 of the Classic Stribeck + Coulomb model. This improvement is possible by adding only one additional parameter to the Stribeck + Coulomb equation. Variant B uses the same reasoning from Variant A and additionally adds an offset to the static friction equation. However, this action results in minimal further improvements to its MSE value and features only an 0.02% improvement compared to the Variant A model.

A 1000 additional local optimization for each model show the robustness of the global optimization results from Table 2 test each model. The starting point for these additional optimizations is randomly constructed in the bounds of 0.0001 to 20 for each

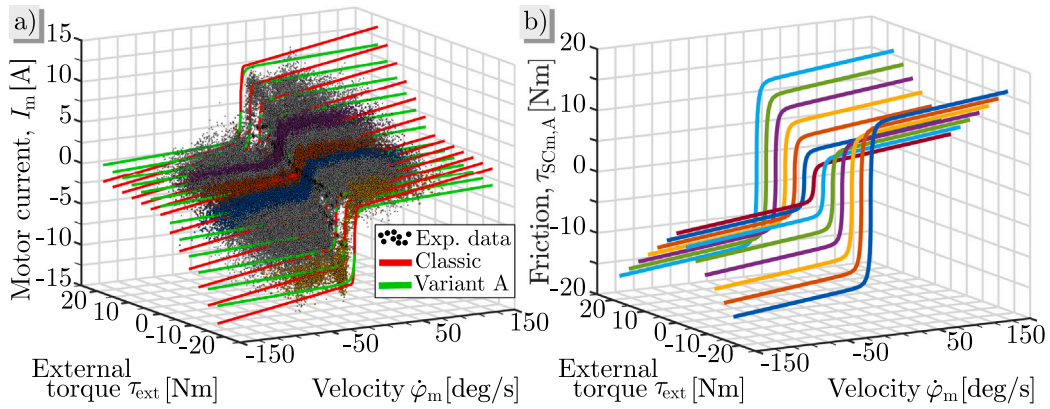


Fig. 12. The theoretical motor current curves. (a) compares the experimental measurements with the use of the Classic and Variant A friction model use. The curves are shown only for a few empirically determined external torque values. The coloured measured points sections and the respective curves are extracted and shown in Fig. 14. (b) shows the respective friction torque curves. (For interpretation of the references to colour in this figure legend, the reader is referred to the web version of this article.)

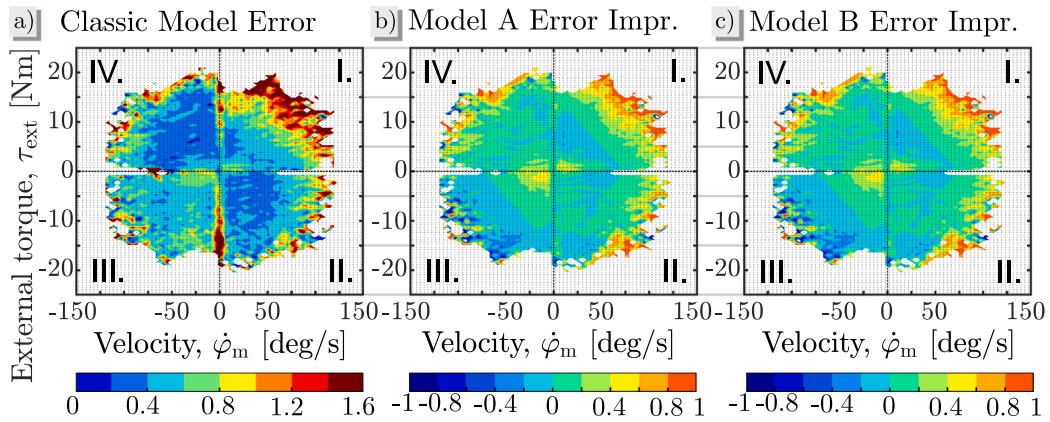


Fig. 13. The mean absolute errors between the actual and theoretical current calculations in the torque/velocity space. The absolute mean error is calculated for the closest measurement points at each grid point. In (a), the current calculation relies on the classical friction model. Contrary to that, (b) and (c) show the improvement/decrease of the modelling error when using either Model A or Model B towards the values in (a). For easier referencing, four quadrants of operation are also marked with Roman numerals.

parameter. Fig. 11 gathers the results and compares the local minimum results to the previous global minimum. As seen, there exist several local solutions for each model. However, the global optimum found with the global optimization corresponds with the minimum solution of the additional local optimizations showing that the solution is robust. While these additional optimizations do not prove the lack of better solutions, the required computing resources outweigh potential improvements gained with further optimizations.

Fig. 12 shows the resulting current and friction curves. In particular, Fig. 12a shows the experimental data points, the resultant Variant A model curves in green colour and the classic model curves in red. Observe how the Variant A model provides an excellent fit to the data. Contrary to that, the classic model features a more aggressive viscous friction behaviour, i.e., the friction is higher than Variant A at higher velocity magnitudes. Fig. 12b shows the systems friction, as approximated with Variant A friction model. Observe how the torque required to overcome friction is very close in magnitude to the external load.

Fig. 13 shows the mean absolute error between the actual current measurements and the theoretical current calculations using a specific model. Fig. 13a shows the errors when using a classic friction model. Contrary to that, Fig. 13b,c shows the improvement towards the errors in Fig. 13a. Following Fig. 13b,c, the use of the Variant A model improves the errors in the centre of the torque/velocity space. Use of the Variant A model results in improvement also in quadrants I, II, and IV of graphs in Fig. 13b,c. However, quadrant III appears different from the other three. In quadrant III there are some red points where use of the Variant A model improved the performance, there are also areas where the modelling error increased. This difference could be attributed to the tension mechanism of the timing belt transmission. The timing belt transmission is tensioned with a spring-loaded lever. At higher torques this lever also contributes to the elasticity of the system, but differs for positive and negative loads.

For further analysis, four of the model curves from Fig. 12 are shown in a velocity projection in Fig. 14 with their respective experimental data points segments. Fig. 14 shows a subtle difference between the data approximation with the use of different

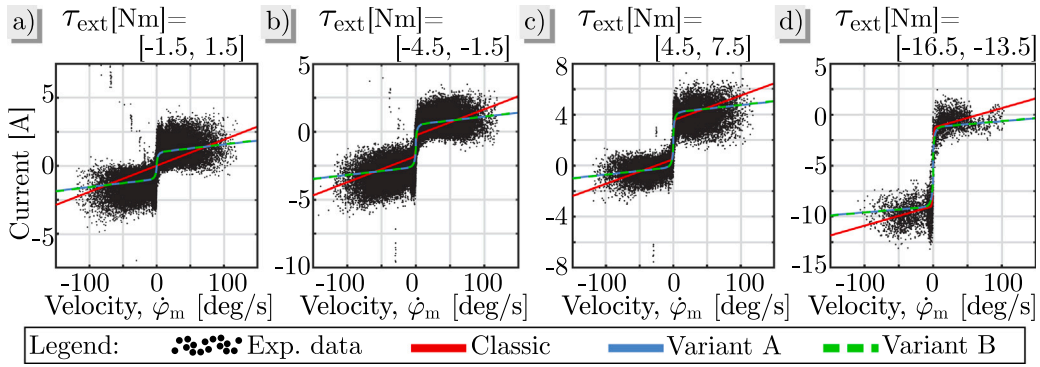


Fig. 14. Measurement points at the specified external torque intervals. The corresponding current curves are shown with the underlying classic friction model, Variant A and Variant B models. (a), (b), (c) and (d) correspond to external torque segments from Fig. 12.

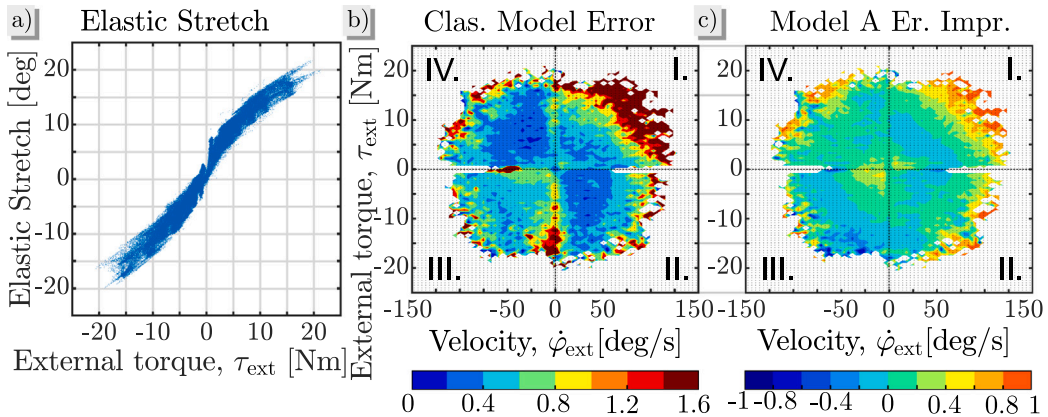


Fig. 15. Elastic stretch and error in relation to joint velocity. (a) shows the elastic deformation of the exoskeleton joint, detected as the difference between external position sensing and motor position sensing. (b) shows the torque/velocity modelling error of motor current when relying on the classical friction model. Furthermore, (c) shows the error improvement when using the Variant A friction model. Note that here, the motor velocity is used to acquire the errors and joint velocity (external velocity) to plot them.

friction models. Fig. 14a,b show that the classic Stribeck + Coulomb model cannot approximate the experimental data at small magnitudes of external load. The reason lies in the limited representation capability since the model assumes that the Coulomb friction component is zero at low or zero external load. However, this is not true for the actuation system of the presented exoskeleton device. Due to this discrepancy at lower external load magnitudes, the classic model approximates the data more aggressively at higher external load magnitudes. This can be seen in Fig. 14c,d, where the friction magnitude increases more rapidly with the increasing velocity. Contrary to the classic model, the Variant A and Variant B models capture the data better.

The experimental data contains a few outlier data points, see Fig. 14a,b,c. However, all the models are not visibly affected by them. Another observation is that while the general shape matches the measurements well, the computed signal is smoother at the zero velocity transition, unlike the theoretical model in Fig. 7. Although step discontinuities are observed in the experimental data in Fig. 14b,c,d, the optimization enforces smoother transitions. The discontinuities are challenging to match with the optimization algorithms because the zero velocity transitions in the actual data happen more smoothly. Consequently, the friction model curves have a rounder shape. However, the cause could lie in the elasticity or compliance of the Bowden cable system that acts as a filter for shock loads [5].

This elasticity is best shown in Fig. 15a. The elastic stretch correlates well with the external torque, i.e., external load. Further research is required to see how robust the stretch relation is in regards to cable bending and cable preload. Furthermore, Fig. 15b, c show the same error from Fig. 13 but now depicted in relation joint velocity ($\dot{\varphi}_{ext}$). Note that the same friction model was used with motor velocity as calculation input. While there are subtle differences between Figs. 15b and 13a, no major conclusion are possible from the view of joint velocity.

Finally, Fig. 16 collects the actuator model parameters and shows their relation to the external load. Overall, the numerical values collected support the above observations. The values of the actuator constant k_a are similar in all three cases. And as expected, the τ_c component features an offset in Variant A and B, and no offset in the classic model. For the reasons explained above, the classic model features a much higher viscous friction parameter k_v , as in Variant A and B. The classic and Variant A models feature no offset in static friction, while the Variant B also features the offset. The classic model also detects higher static friction than the

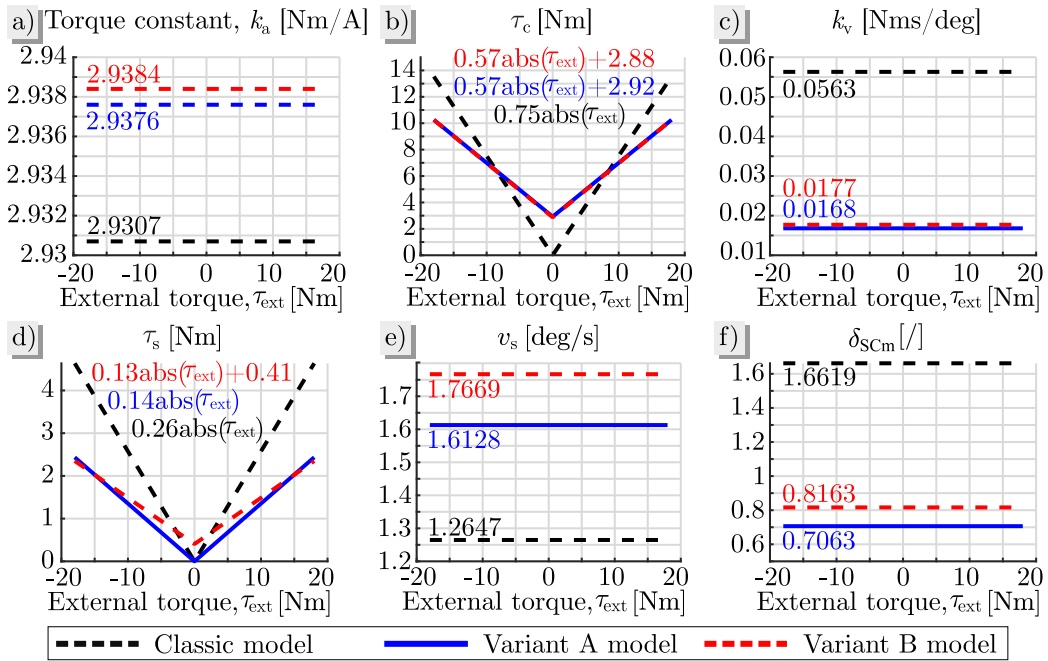


Fig. 16. This figure shows the resulting optimal values for the actuator model parameters and the respective underlying friction models.

other two models. The parameters v_s and parameter δ_{SCm} differ in their values for the different friction models, which culminated in varying levels of smoothness of friction curves at the discrete non-linearity for the different friction models. The approximation curves in Fig. 14 feature a different curvature between the separate models.

The proposed model allows two ways of use. First, its mathematical relation features parameter extension capabilities to capture cable preload and bending behaviour on friction. A model with good descriptive capabilities could then be used as a feedforward current control signal.

Secondly, the proposed friction model could improve sensor signal quality, i.e., integrated load cell measurements and cable stretch measurements. The potential sensor fusion of these signals requires further investigation; however, initial experiments show potential. Towards this end, additional sensors are planned in the exoskeleton device, i.e. a second absolute encoder to measure the cable stretch and two load cells to measure the cable preload. The addition of these sensors allows for further investigation of the above potential uses.

5. Conclusions

The first part of this paper proposes several mechanical solutions for a cable-driven upper-body exoskeleton device and its actuation. The gathered experimental data shows that system is subject to non-neglectable amounts of friction. However, it also indicates that the proposed actuation unit can generate an external 20 N m torque at the actuated joint, which is enough for assistance in activities of daily living.

The second part of the paper focuses on the modelling aspects of friction and actuation from the actual exoskeleton data. The results expose the inability of the classic Stribeck + Coulomb friction model to approximate experimental data at smaller external load magnitudes. And consequently, it also over-approximates the viscous friction component at higher velocity magnitudes.

Contrary to that, the offset based friction model in question, i.e., Variant A model, shows a better approximation of the exoskeleton data. An additional offset parameter in the Coulomb friction component improves its capability, and the resulting model features a 15% improvement compared to the classic Stribeck + Coulomb model. This improvement is evident at the lower magnitudes of external load, where the classical model cannot approximate the friction effects.

These conclusions are important since other more advanced friction models rely on the same Coulomb friction definition as the Classic Stribeck + Coulomb model and could improve with the addition of the offset parameter.

Out future work envisions a study of the effects of preload and cable-bending on parameters of the proposed current/friction model and the development of an extension of the proposed friction models to accommodate these behaviours.

Declaration of competing interest

The authors declare that they have no known competing financial interests or personal relationships that could have appeared to influence the work reported in this paper.

Acknowledgements

This research was funded by Slovenian Research Agency program group Automation, Robotics, and Biocybernetics (P2-0076) and young researcher grant PR-06812 as well as DAAD - German Academic Exchange Service (Research Grants - Short-Term Grants, 2018, 57381332) and by the Carl Zeiss Foundation through the JuBot project.

References

- [1] M. Sanchez-Villamanan, J. Gonzalez-Vargas, D. Torricelli, J. Moreno, J. Pons, Compliant lower limb exoskeletons: A comprehensive review on mechanical design principles, *J. NeuroEng. Rehabil.* 16 (1) (2019) 55, <http://dx.doi.org/10.1186/s12984-019-0517-9>.
- [2] M.A. Gull, S. Bai, T. Bak, A review on design of upper limb exoskeletons, *Robotics* 9 (1) (2020) 16, <http://dx.doi.org/10.3390/robotics9010016>.
- [3] A. Gupta, A. Singh, V. Verma, A.K. Mondal, M.K. Gupta, Developments and clinical evaluations of robotic exoskeleton technology for human upper-limb rehabilitation, *Adv. Robot.* (2020) 1–18, <http://dx.doi.org/10.1080/01691864.2020.1749926>.
- [4] G. Bao, L. Pan, H. Fang, X. Wu, H. Yu, S. Cai, B. Yu, Y. Wan, Academic review and perspectives on robotic exoskeletons, *IEEE Trans. Neural Syst. Rehabil. Eng.* 27 (11) (2019) 2294–2304, <http://dx.doi.org/10.1109/TNSRE.2019.2944655>.
- [5] A. Albu-Schaffer, O. Eiberger, M. Grebenstein, S. Haddadin, C. Ott, T. Wimbock, S. Wolf, G. Hirzinger, Soft robotics, *IEEE Robot. Autom. Mag.* 15 (3) (2008) 20–30, <http://dx.doi.org/10.1109/MRA.2008.927979>.
- [6] A. Bicchi, G. Tonietti, Fast and "soft-arm" tactics [robot arm design], *IEEE Robot. Autom. Mag.* 11 (2) (2004) 22–33, <http://dx.doi.org/10.1109/MRA.2004.1310939>.
- [7] R.C. Browning, J.R. Modica, R. Kram, A. Goswami, The effects of adding mass to the legs on the energetics and biomechanics of walking, *Med. Sci. Sports Exerc.* 39 (3) (2007) 515–525, <http://dx.doi.org/10.1249/mss.0b013e31802b3562>.
- [8] D. Braun, M. Howard, S. Vijayakumar, Optimal variable stiffness control: formulation and application to explosive movement tasks, *Auton. Robots* 33 (3) (2012) 237–253, <http://dx.doi.org/10.1007/s10514-012-9302-3>.
- [9] M. Dežman, A. Gams, Rotatable cam-based variable-ratio lever compliant actuator for wearable devices, *Mech. Mach. Theory* 130 (2018) 508–522, <http://dx.doi.org/10.1016/j.mechmachtheory.2018.09.006>.
- [10] G. Lee, Y. Ding, I.G. Bujanda, N. Karavas, Y.M. Zhou, C.J. Walsh, Improved assistive profile tracking of soft exosuits for walking and jogging with off-board actuation, in: 2017 IEEE/RSJ International Conference on Intelligent Robots and Systems (IROS), IEEE, 2017, pp. 1699–1706, <http://dx.doi.org/10.1109/iros.2017.8205981>.
- [11] L. Cappello, A. Pirrera, P. Weaver, L. Masia, A series elastic composite actuator for soft arm exosuits, in: 2015 IEEE International Conference on Rehabilitation Robotics (ICORR), IEEE, 2015, pp. 61–66, <http://dx.doi.org/10.1109/icorr.2015.7281176>.
- [12] J. Sanjuan, A.D. Castillo, M.A. Padilla, M.C. Quintero, E. Gutierrez, I.P. Sampayo, J.R. Hernandez, M.H. Rahman, Cable driven exoskeleton for upper-limb rehabilitation: A design review, *Robot. Auton. Syst.* 126 (2020) 103445, <http://dx.doi.org/10.1016/j.robot.2020.103445>.
- [13] J. Dittli, U. Hofmann, T. Bützer, O. Lamercy, R. Gassert, Remote actuation systems for fully wearable assistive devices: requirements, selection, and optimization for out-of-the-lab application of a hand exoskeleton, *Front. Robot. AI* 7 (2020) 187, <http://dx.doi.org/10.3389/frobt.2020.596185>.
- [14] J.F. Veneman, R. Ekkelenkamp, R. Kruidhof, F.C. van der Helm, H. van der Kooij, A series elastic-and bowden-cable-based actuation system for use as torque actuator in exoskeleton-type robots, *Int. J. Robot. Res.* 25 (3) (2006) 261–281, <http://dx.doi.org/10.1177/0278364906063829>.
- [15] S. Wang, J. Li, R. Zheng, A resistance compensation control algorithm for a cable-driven hand exoskeleton for motor function rehabilitation, in: International Conference on Intelligent Robotics and Applications, Springer, 2010, pp. 398–404, http://dx.doi.org/10.1007/978-3-642-16587-0_37.
- [16] T. Noda, T. Teramae, B. Ugurlu, J. Morimoto, Development of an upper limb exoskeleton powered via pneumatic electric hybrid actuators with bowden cable, in: 2014 IEEE/RSJ International Conference on Intelligent Robots and Systems, IEEE, 2014, pp. 3573–3578, <http://dx.doi.org/10.1109/IROS.2014.6943062>.
- [17] W. Wei, Z. Qu, W. Wang, P. Zhang, F. Hao, Design on the bowden cable-driven upper limb soft exoskeleton, *Appl. Bionics Biomech.* 2018 (2018) <http://dx.doi.org/10.1155/2018/1925694>.
- [18] U. Jeong, K. Kim, S.-H. Kim, H. Choi, B.D. Youn, K.-J. Cho, Reliability analysis of a tendon-driven actuation for soft robots, *Int. J. Robot. Res.* 40 (1) (2021) 494–511, <http://dx.doi.org/10.1177/0278364920907151>.
- [19] B.K. Dinh, M. Xiloyannis, L. Cappello, C.W. Antuvan, S.-C. Yen, L. Masia, Adaptive backlash compensation in upper limb soft wearable exoskeletons, *Robot. Auton. Syst.* 92 (2017) 173–186, <http://dx.doi.org/10.1016/j.robot.2017.03.012>.
- [20] S. Yeo, G. Yang, W. Lim, Design and analysis of cable-driven manipulators with variable stiffness, *Mech. Mach. Theory* 69 (2013) 230–244, <http://dx.doi.org/10.1016/j.mechmachtheory.2013.06.005>.
- [21] A.T. Asbeck, K. Schmidt, C.J. Walsh, Soft exosuit for hip assistance, *Robot. Auton. Syst.* 73 (2015) 102–110, <http://dx.doi.org/10.1016/j.robot.2014.09.025>.
- [22] J. Kim, G. Lee, R. Heimgartner, D.A. Revi, N. Karavas, D. Nathanson, I. Galiana, A. Eckert-Erdheim, P. Murphy, D. Perry, et al., Reducing the metabolic rate of walking and running with a versatile, portable exosuit, *Science* 365 (6454) (2019) 668–672, <http://dx.doi.org/10.1126/science.aav7536>.
- [23] S. Lessard, P. Pansodtee, A. Robbins, J.M. Trombadore, S. Kurniawan, M. Teodorescu, A soft exosuit for flexible upper-extremity rehabilitation, *IEEE Trans. Neural Syst. Rehabil. Eng.* 26 (8) (2018) 1604–1617, <http://dx.doi.org/10.1109/TNSRE.2018.2854219>.
- [24] Y. Ding, I. Galiana, A.T. Asbeck, S.M.M. De Rossi, J. Bae, T.R.T. Santos, V.L. De Araujo, S. Lee, K.G. Holt, C. Walsh, Biomechanical and physiological evaluation of multi-joint assistance with soft exosuits, *IEEE Trans. Neural Syst. Rehabil. Eng.* 25 (2) (2016) 119–130, <http://dx.doi.org/10.1109/TNSRE.2016.2523250>.
- [25] A.T. Asbeck, S.M. De Rossi, I. Galiana, Y. Ding, C.J. Walsh, Stronger, smarter, softer: next-generation wearable robots, *IEEE Robot. Autom. Mag.* 21 (4) (2014) 22–33, <http://dx.doi.org/10.1109/MRA.2014.2360283>.
- [26] U. Jeong, K.-J. Cho, Feedforward friction compensation of Bowden-cable transmission via loop routing, in: 2015 IEEE/RSJ International Conference on Intelligent Robots and Systems (IROS), IEEE, 2015, pp. 5948–5953, <http://dx.doi.org/10.1109/iros.2015.7354223>.
- [27] A. Schiele, P. Letier, R. Van Der Linde, F. Van Der Helm, Bowden cable actuator for force-feedback exoskeletons, in: 2006 IEEE/RSJ International Conference on Intelligent Robots and Systems, IEEE, 2006, pp. 3599–3604, <http://dx.doi.org/10.1109/iros.2006.281712>.
- [28] P. Herbin, M. Pajor, The torque control system of exoskeleton ExoArm 7-DOF used in bilateral teleoperation system, *AIP Conf. Proc.* 2029 (1) (2018) 020020, <http://dx.doi.org/10.1063/1.5066482>.
- [29] A.S. Kernbaum, R. Kornbluh, Efficient bowden cable system, 2015, U.S. Patent US20190128314A1.
- [30] Y. Yun, P. Agarwal, J. Fox, K.E. Madden, A.D. Deshpande, Accurate torque control of finger joints with UT hand exoskeleton through bowden cable SEA, in: 2016 IEEE/RSJ International Conference on Intelligent Robots and Systems (IROS), IEEE, 2016, pp. 390–397, <http://dx.doi.org/10.1109/iros.2016.7759084>.
- [31] U. Jeong, K.-J. Cho, A feasibility study on tension control of bowden-cable based on a dual-wire scheme, in: 2017 IEEE International Conference on Robotics and Automation (ICRA), IEEE, 2017, pp. 3690–3695, <http://dx.doi.org/10.1109/ICRA.2017.7989424>.
- [32] U.A. Hofmann, T. Bützer, O. Lamercy, R. Gassert, Design and evaluation of a bowden-cable-based remote actuation system for wearable robotics, *IEEE Robot. Autom. Lett.* 3 (3) (2018) 2101–2108, <http://dx.doi.org/10.1109/LRA.2018.2809625>.

- [33] V. Agrawal, W.J. Peine, B. Yao, Modeling of transmission characteristics across a cable-conduit system, *IEEE Trans. Robot.* 26 (5) (2010) 914–924, <http://dx.doi.org/10.1109/tro.2010.2064014>.
- [34] S.H. Collins, M. Kim, T. Chen, T. Chen, An ankle-foot prosthesis emulator with control of plantarflexion and inversion-eversion torque, in: 2015 IEEE International Conference on Robotics and Automation (ICRA), IEEE, 2015, pp. 1210–1216, <http://dx.doi.org/10.1109/ICRA.2015.7139345>.
- [35] Z. Sun, Z. Wang, S.J. Phee, Elongation modeling and compensation for the flexible tendon–sheath system, *IEEE/ASME Trans. Mechatronics* 19 (4) (2013) 1243–1250, <http://dx.doi.org/10.1109/TMECH.2013.2278613>.
- [36] P. Maurice, S. Ivaldi, J. Babic, J. Camernik, D. Gorjan, B. Schirrmeister, J. Bornmann, L. Tagliapietra, C. Latella, D. Pucci, L. Fritzsche, Objective and subjective effects of a passive exoskeleton on overhead work, *IEEE Trans. Neural Syst. Rehabil. Eng.* 28 (1) (2020) 152–164, <http://dx.doi.org/10.1109/tnsre.2019.2945368>.
- [37] M. Müser, Valentin I. Popov: Contact mechanics and friction: Physical principles and applications, *Tribol. Lett.* 40 (3) (2010) 395, <http://dx.doi.org/10.1007/978-3-642-10803-7>.
- [38] D. Chen, Y. Yun, A.D. Deshpande, Experimental characterization of bowden cable friction, in: 2014 IEEE International Conference on Robotics and Automation (ICRA), IEEE, 2014, pp. 5927–5933, <http://dx.doi.org/10.1109/ICRA.2014.6907732>.
- [39] Z. Wang, S. Rho, C. Yang, F. Jiang, Z. Ding, C. Yi, B. Wei, Active loading control design for a wearable exoskeleton with a bowden cable for transmission, *Vol. 10, no. 6, 2021*, p. 108. <http://dx.doi.org/10.3390/act10060108>.
- [40] T. Nef, M. Mihelj, R. Riener, ARMin: A robot for patient-cooperative arm therapy, *Med. Biol. Eng. Comput.* 45 (9) (2007) 887–900, <http://dx.doi.org/10.1007/s11517-007-0226-6>.
- [41] B. Drury, *Control Techniques Drives and Controls Handbook*, Vol. 35, IET, 2001, <http://dx.doi.org/10.1049/pbpo057e>.
- [42] H. Yuan, L. Zhou, W. Xu, A comprehensive static model of cable-driven multi-section continuum robots considering friction effect, *Mech. Mach. Theory* 135 (2019) 130–149, <http://dx.doi.org/10.1016/j.mechmachtheory.2019.02.005>.
- [43] H. Olsson, K. Åström, C.C. de Wit, M. Gäfvert, P. Lischinsky, Friction models and friction compensation, *Eur. J. Control* 4 (3) (1998) 176–195, [http://dx.doi.org/10.1016/s0947-3580\(98\)70113-x](http://dx.doi.org/10.1016/s0947-3580(98)70113-x).
- [44] Y. Liu, J. Li, Z. Zhang, X. Hu, W. Zhang, Experimental comparison of five friction models on the same test-bed of the micro stick-slip motion system, *Mech. Sci.* 6 (1) (2015) 15–28, <http://dx.doi.org/10.5194/ms-6-15-2015>.
- [45] S. Andersson, Friction and wear simulation of the wheel–rail interface, in: *Wheel–Rail Interface Handbook*, Elsevier, 2009, pp. 93–124, <http://dx.doi.org/10.1533/9781845696788.1.94>.
- [46] U. Jeong, K.-J. Cho, Control of a bowden-cable actuation system with embedded boasensor for soft wearable robots, *IEEE Trans. Ind. Electron.* 67 (9) (2019) 7669–7680, <http://dx.doi.org/10.1109/TIE.2019.2945212>.